Published in final edited form as:
Icarus. 2019 July ; 326: 10–17. doi:10.1016/j.icarus.2019.01.027.

Using the density of Kuiper Belt Objects to constrain their composition and formation history

C. J. Bierson[a,*], **F. Nimmo**[a]

[a]Department of Earth and Planetary Sciences, UC Santa Cruz, Santa Cruz, CA 95064, USA

Abstract

Telescopic observations of Kuiper Belt objects have enabled bulk density determinations for 17 objects. These densities vary systematically with size, perhaps suggesting systematic variations in bulk composition. We find this trend can be explained instead by variations in porosity arising from the higher pressures and warmer temperatures in larger objects. We are able to match the density of 14 of 17 KBOs within their 2σ errors with a constant rock mass fraction of 70%, suggesting a compositionally homogeneous, rock-rich reservoir. Because early ^{26}Al would have removed too much porosity in small (~100 km) KBOs we find the minimum formation time to be 4 Myr after solar system formation. This suggests that coagulation, and not gravitational collapse, was the dominant mechanism for KBO formation. We also use this model to make predictions for the density of Makemake, 2007 OR_{10}, and MU_{69}

Keywords

Kuiper Belt; Solar System Formation; Thermal Evolution; Density; Porosity

1. Introduction

As of this writing there are 17 Kuiper Belt systems in which the orbit of the secondary has been determined well enough to meaningfully estimate the system mass (Table A.2). In these cases, with the addition of radii measurements from either occultation or direct imaging, the primary's density can be determined. In small KBOs the uncertainty in radius can be large, leading to a large uncertainty in density. Despite this there is a clear systematic trend of larger objects also having a higher density (Brown, 2012).

There are at least three mechanisms that could generate the oberved KBO density distribution. The first is that large KBOs could contain higher density ice phases. However, the low internal pressures in even the largest KBOs (Grundy et al., 2007; Brown, 2012), along with an absence of any evidence for such high-pressure phases in Pluto (McKinnon et al., 2017), rules out this possibility. The second is there could be a compositional difference between small and large KBOs. This would require smaller KBOs to be significantly more ice rich than their larger counterparts (Brown, 2012). The most commonly discussed mechanism to generate such a difference is large disruptive impacts. Modeling has been

*Corresponding author.

done to estimate the effect impacts could have on the bulk density of particular systems (Leinhardt et al., 2010; Canup, 2011; Barr and Schwamb, 2016) but not on the overall density distribution. Estimates using existing scaling laws suggest that impacts are an implausible explanation due to the large fraction of material that would need to be removed from the system (Brown, 2012). A compositional gradient could also arise if larger bodies could lose volatiles preferentially due to accretional heating (McKinnon and Mueller, 1988; Bierson et al., 2018) but we show below that this mechanism is not plausible (see Appendix C). The third possibility is that small KBOs contain substantial porosity (Brown, 2012) not present in larger bodies, and is the focus of this work.

Experimental work has shown a series of processes that remove macro-porosity in different temperature-pressure regimes. Below 1 MPa significant macro porosity can be maintained in cold water ice (Durham et al., 2005; Yasui and Arakawa, 2009). Between 1 and 10's of MPa brittle failure begins to cause the porosity to fall rapidly. In this regime pore closure is independent of temperature. The degree of pore closure due to brittle failure is dependent on the rock mass fraction. At pressures greater than 10's of MPa ductile deformation dominates. In this high pressure regime compaction depends on both temperature and rock mass fraction. Durham et al. (2005) found that pure water ice at temperatures of 77 K could support porosity of 10%–20% beyond 100 MPa. In contrast Yasui and Arakawa (2009) found pure water ice samples at 260 K would contain only ~1% porosity at 30 MPa.

In this work we test if porosity is able to explain the observed density distribution of KBOs. This is done with a model of KBO thermal evolution coupled with the porosity evolution. We examine the sensitivity of these results to the KBO rock mass fraction and formation time. We find that the observed density distribution can be well fit with a nearly uniform rock mass fraction. We also find that small KBOs (~ 100 km) must have formed after the decay of ^{26}Al to maintain their high porosity. We discuss the implications of these results for KBO formation.

2. Model

We use a 1D model to probe the effect of the two different pore-closure processes on the bulk density. All model runs begin with an undifferentiated KBO that has an initial bulk porosity ϕ_0 and rock mass fraction $f_m = M_s/(M_s + M_i)$. Here M_s is the mass of the silicates and M_i is the mass of the ice. For each model run the effect of brittle failure is calculated followed by the thermal-ductile pore closure modeling.

Brittle failure is assumed to take place on geologically rapid timescales and is modeled following the empirical results of Yasui and Arakawa (2009). This is done by iteratively calculating the internal pressure and updating the ice and silicate porosity via

$$\phi_i(P) = \max(\phi_0 \exp(b_1 P), \phi_c) \quad (1)$$

$$\phi_s\left(P\right) = \min\left(\phi_0 P^{b_2}, \phi_0\right) \quad (2)$$

where P is the local lithostatic pressure in MPa. The value ϕ_c is the assumed porosity that can be supported by matrix in cold conditions (Durham et al., 2005). Values for the empirical constants used are given in Table 1. These components are then mixed by their volume fractions to get the bulk porosity of each layer. Recalculation of the pressure profile and updating of the porosity profile is iterated until the porosity profile converges. This sets the initial porosity profile for the thermal modeling.

Modeling the subsequent evolution of the porous structure of KBOs is handled by the thermal evolution model of Bierson et al. (2018). The numerical methods used are presented in Appendix B. This model assumes that porosity is primordial and removed over time. The final porosity structure is then dependent on the thermal history. Following Besserer et al. (2013) we model the change in porosity as a function of pressure (P) and viscosity (η) via

$$\frac{d\phi}{dt} = \phi \frac{P}{\eta(T)}. \tag{3}$$

Here the ice viscosity is taken to be Newtonian and is assumed to vary as

$$\eta\left(T\right) = \eta_0 \exp\left(\frac{Q}{R_g T} - \frac{Q}{R_g T_0}\right) \tag{4}$$

where Q is the activation energy, R_g is the gas constant and η_0 is the reference viscosity at T_0 (Table 1). It was shown by Besserer et al. (2013) that equation (3) provides a reasonable approximation to more complicated pore-closure models (Eluszkiewicz, 1990; Leliwa-Kopystyński and Kossacki, 2000).

This model was updated from Bierson et al. (2018) to include short-lived radioisotopes. The method by which porosity affects thermal conductivity has also been updated. The effect of porosity on thermal conductivity is one of the largest uncertainties in modeling high porosity objects. The true conductivity of a porous mixture depends on the geometry of the matrix (how interconnected the pores are) and the effective thermal conductivity of the pore space itself. While there are no direct constraints on the thermal conductivity of KBOs, there exists a wealth of theoretical work to bound the value. A detailed review of different physical models is given in Carson et al. (2005).

In this work the thermal conductivity is computed for each timestep as follows. We begin by assuming the rock-ice matrix itself is well mixed. As such we use the parallel model to combine an assumed constant silicate conductivity and temperature dependent ice conductivity (see values in Table 1).

$$k_0\left(f_{rock}, T\right) = k_s\left(f_m \frac{\rho_s}{\rho}\right) + k_{ice}\left(1 - f_m \frac{\rho_s}{\rho}\right) \tag{5}$$

We then assume heat transfer through the porosity itself is highly inefficient and apply the parallel model via

$$k(\phi) = k_0(f_{rock}, T)(1 - \phi) \tag{6}$$

The parallel model is the upper bound for the thermal conductivity in a solid medium. Any lower values chosen for the thermal conductivity would lead to higher densities (more porosity removed) for smaller objects. Radiation may slightly enhance the heat transfer in a porous material. Shoshany et al. (2002) calculated the effective thermal conductivity including radiation and the parallel model is in the middle of the range of values they predict. Changing our thermal conductivity model to the maximum conductivity model of Shoshany et al. (2002) results in at most an 8% decrease in predicted density at intermediate (400 km) radii, and less at larger or smaller radii. Neglecting the effect of porosity on thermal conductivity entirely results in at most a 10% change in the final density. This change is too small to alter any of our conclusions.

2.1. Parameters and sensitivity

Table 1 gives the nominal values for all the parameters used in this modeling. These values are generally taken from Bierson et al. (2018). The new parameters are those for the brittle failure modeling taken from Durham et al. (2005) and Yasui and Arakawa (2009). The other important controlling parameter is the initial porosity. Here a nominal value of 60% is used as this gives an object with f_m = 70% a density of ~750 kg/m^3. This high porosity is consistent with measurements made for asteroids, which Baer et al. (2011) find exhibit a range of porosity from 10%–70% for radii up to ~150 km. While porosity is difficult to infer for comets as we do not know the grain density, the bulk density of comets like 67P/Churyumov-Gerasimenko (532 ± 7 kg m^3, Jorda et al. (2016)) imply a porosity of $>$40%.

Our model has very little sensitivity to most of the parameters in Table 1. A factor of two change in C_p leads to a 4% change in the bulk density (~50 kg m^3). Changing η_0 to 10^{17} Pa s also changes the final density by up to 4%. Changing the initial porosity changes the density of small KBOs (as expected) but does not notably change the radius at which density begins to increase. While each of these parameters may change the rate of change or the timing of when porosity closes, the final bulk density is a robust outcome of our model runs.

2.2. Processes not modeled

The modeling in this work does not include melt production, differentiation, convection, impacts, and tidal heating. Here we discuss each of these process in turn and their potential impact on our results. Melting to form a subsurface ocean will increase the bulk density while the ocean is present, but the effect is small and will disappear once the ocean freezes (McKinnon et al., 2017; Bierson et al., 2018). Differentiation redistributes the mass within the body; however, because no mass is lost the bulk density is unchanged. As differentiation occurs a small amount of extra gravitational energy will be released which is not included here (Desch et al., 2009; Malamud and Prialnik, 2015). The redistribution of ice and silicates will also change the magnitude of compression but given the low internal pressures of KBOs we expect this to have only a minor effect (Bierson et al., 2018). Since differentiation redistributes the heat source (silicates) towards the center of the body, higher internal temperatures will result, making our porosity estimates conservatively high. Convection will remove heat more rapidly than in our conductive models, but if ice is warm enough to convect, all porosity will already have been removed.

In a high porosity surface, impacts will also reduce the bulk porosity. This effect is limited to the upper tens of kilometers (Milbury et al., 2015), small compared to the size of objects considered here. It is possible that during the formation of larger KBOs, impacts may have removed porosity in a significant fraction of the outer ice shell. Large disruptive impacts into differentiated KBOs could change f_m and are further discussed in section 3.

All the KBOs discussed here are either in binary systems or experienced capture (Goldreich et al., 1989; Agnor and Hamilton, 2006). Because of this tidal heating may have been an extra energy source. The amount of energy and its importance to the overall thermal evolution is dependent on the initial orbital configuration and internal structure of the KBOs (Saxena et al., 2018).

The important point for this work is that all these processes have the same net effect of removing more porosity than predicted by our model. Similarly, we assume an upper limit for the thermal conductivity at a given porosity. A lower thermal conductivity would allow more heat to build up in the interior, removing additional porosity. As a result our model runs represent a *lower bound* on the bulk density (the most porosity that can be retained).

In this work we also assume that the 'ice' component is dominated in composition by H_2O. Depending on their formation conditions, some KBOs may have incorporated ices during formation such as N_2, NH_3, CO, CO_2, and CH_4. Most of these ices have densities close to that of water ice (950, 850, 1000, 1000–1600, 500 kg/m^3 respectively) and so cannot have a significant effect on the bulk density at reasonable concentrations (Satorre et al., 2008, 2013; Umurhan et al., 2017). For example, to change the bulk density by ~300 kg/m^3 through the addition methane (the ice with the lowest density) would require adding ~8% of the total body mass. There is also no clear reason these compositional differences would depend on size, the main focus of this work.

3. Results

A comparison of our model results with the observed KBO values are shown in Figure 1a. Our model predicts that the transition from small porous objects to dense KBOs occurs quickly between a radius of 200km-500km. This transition radius is set by the balance between heat production (which depends on f_m and radioactive half-life) and conductive heat loss (which depends on the body size). An analogous argument has been made for understanding the minimum size of differentiation in asteroids (Grimm and McSween Jr, 1993).

Around this transition diameter internal temperatures begin to reach or exceed the melting point of water (red stars). For the reasons presented in Section 2.2 these points are more likely to underestimate the bulk density. The maximum bulk density for a given f_m (neglecting compression) is shown by the dashed lines. This is the density an object of a given f_m would have with no porosity. We estimate the f_m for each KBO in Figure 1b with error bars that include the observational uncertainty and in addition treat our model and zero porosity values as limiting cases (see Figure caption for details). This is a conservative

estimate that likely overestimates our error particularly for small KBOS and on the lower limits.

For a rock mass fraction of 70% our model matches the density observations for ten of seventeen KBOs within 1σ and fourteen of seventeen within 2σ (Figure 1b). The three objects not well fit by this model are Triton, Eris, and 2002 UX_{25}. Eris and Triton both require $f_m > 70\%$. Triton's high rock fraction might be a consequence of the extreme heating it experienced during capture (Goldreich et al., 1989). There is also a hint that scattered disk objects may have a higher f_m compared with classical KBOs. This could be due to more energetic collisions caused by their more dynamically excited orbits; such collisions will have preferentially removed the ice-rich mantles of differentiated objects, potentially explaining the higher rock fraction of Eris (Lissauer and Stewart, 1993; Barr and Schwamb, 2016). 2002 UX_{25} is below our expected density. We are not aware of any processes that might significantly lower the bulk density without lowering f_m. Our model predicts that $f_m \sim 50\%$ for 2002 UX_{25}. It is worth noting that at present no light curve or occultation measurements have been used to constrain the shape of 2002 UX_{25}. If it is significantly non-spherical in shape this could lead to an overestimation of its volume, and thereby an underestimation of the density. Whatever the case, this object remains enigmatic but is also only a single data point.

We can also place a constraint on the formation time of KBOs as follows. The earlier in solar system history KBOs form the more short lived radiogenic isotopes will be incorporated. It is these isotopes that are responsible for differentiation of small asteroids (Grimm and McSween Jr, 1993); in the case of KBOs, if these objects form too early, sufficient ^{26}Al will be present that all porosity is removed. We assume chondritic abundances of ^{26}Al, ^{60}Fe, ^{53}Mn in the silicate component of modeled KBOs (Table A.3). Figure 2 shows the final density of modeled KBOs as a function of their formation time. If a small KBO with $f_m = 0.7$ forms before 5 Myr after CAI the internal porosity will be removed by the heat from the decay of short lived isotopes (primarily ^{26}Al). At $f_m = 0.5$ this limit is pushed to 4 Myr after CAI. As previously noted other feedbacks would further remove porosity once the object starts to warm. Based on these results we conclude that 4 Myr is a lower bound on the KBO formation time. This is consistent with the modeling of Merk and Prialnik (2006) who found that objects larger than a few kilometers radius reach internal temperatures sufficient for liquid water if formed with ^{26}Al still live. A similar argument has been made in favor of a low ^{26}Al in the small Saturnian satellites(Leliwa-Kopystyński and Kossacki, 2000). This is also consistent with McKinnon et al. (2017) who argue that Pluto couldn't be fully differentiated before the Charon-forming impact, and therefore that Pluto did not form while ^{26}Al was live.

An analogous argument can be made that small, low density KBOs cannot have experienced large amounts of tidal heating. As more precise estimates of the orbits and individual masses of KBO binary systems become available this should allow constraints to be placed on the tidal parameters such as k_2/Q (Saxena et al., 2018).

4. Dicussion

The results above show that small KBOs cannot have formed prior to 4 Ma, as otherwise they would have experienced too much porosity reduction. Placing this timing constraint on the formation of KBOs allows us to test the formation models that have been proposed. There are currently two main models for KBO formation. The coagulation model proposes that KBOs formed from kilometersized precursors that interacted dynamically to form larger bodies (Kenyon, 2002; Kenyon et al., 2008; Schlichting and Sari, 2011). Because of the long orbital periods this process takes tens of millions of years to form the large KBOs. Alternatively the Nesvorný et al. (2010) model proposes that decimeter sized 'pebbles' could be aggregated by the streaming instability to undergo gravitational collapse. This gravitational collapse model naturally forms binary systems which are common in the Kuiper belt and dynamical evidence suggests may have been more common early in the solar system (Petit and Mousis, 2004; Fraser et al., 2017). KBO binaries could form through gravitational interactions (Goldreich et al., 2002) although it remains open if this mechanism is efficient enough to form the inferred number of binary systems.

Because the Nesvorný et al. (2010) model invokes the streaming instability, it requires the presence of a gas disk. Astronomical observations of disks around young systems suggest disk lifetimes of three to ten million years (Haisch et al., 2001; Williams and Cieza, 2011). Constraints from the inner solar system suggest that the gas was present until 4 – 5 Myr after solar system formation (Johnson et al., 2016; Wang et al., 2017; Kruijer et al., 2017). Our results constrain KBO formation to be after 4 – 5 Myr, around the same time the gas disk is dispersing in the inner solar system.

One interpretation of this result could be that the gas disk must have persisted longer in the outer solar system. How plausible this is depends on what mechanism(s) are responsible for removing the gas disk in the outer solar system (Matsuyama et al., 2003). This explanation would also require that KBO formation only occur after 4 Myr; if collapse were operating before 4–5 Myr, small dense KBOs should have formed, but are not observed. The alternative interpretation is that our constraint favors KBO formation via the coagulation model. In this case there is no need for special timing because the ~100 km KBOs naturally form long after the shortlived isotopes are extinct.

This work also has implications for the dynamical environment of the Kuiper Belt. The near constant f_m is in stark contrast with the inner solar system where core mass fractions vary from 2% (the Moon, Weber et al. 2011) to 70% (Mercury, Rivoldini et al. 2009). This suggests that there was much less erosion of material by impacts relative to the inner solar system. This may be due to the fact that giant impacts between KBOs, such as the one that may have formed the Pluto-Charon system, do not necessarily lead to large changes in the bulk composition (Canup, 2011). A relative absence of giant impacts is also consistent with the preponderance of binary systems being formed by long-range dynamical interactions (Goldreich et al., 2002).

Our results suggest that KBOs form a homogenous population, in terms of their bulk composition. While variations in surface color certainly exist, and appear to be related to

dynamical characteristics (Brown, 2012; Dalle Ore et al., 2013; Tegler et al., 2016), we see little evidence of systematic variations in bulk composition, except for a hint that scattered disk objects are more rock-rich (Fig 1b).

Going forward we expect future observations to be able to test the model presented here. Moons have recently been discovered for Makemake (Parker et al., 2016) and 2007 OR_{10} (Kiss et al., 2017) making density measurements likely in the near future. Our results that both of these objects should have bulk densities similar to, or slightly less than, that of Pluto (≈1800 kg m^{-3}). In contrast, if a mass measurement is possible during the New Horizons flyby of 2014 MU_{69} (r~ 30 km) we expect it to have a low density of ~ 750 kg/m^3.

5. Conclusion

We find the density distribution of KBOs is best explained not by variations in composition, but in bulk porosity. KBOs transition from highly porous to having only a surface porous layer when the internal heat production by radioactive decay outpaces the rate of energy transport by thermal conduction. Because the large amount of energy in ^{26}Al would have melted even small KBOs ($r \sim 100$ km) we conclude they must have formed ~5 Myr after CAI. As observations of KBO density are refined and more acquired more narrow constraints will be placed on the range of compositions within the Kuiper Belt.

Acknowledgements

This material is based upon work supported by the National Science Foundation Graduate Research Fellowship under Grant No. NSF DGE 1339067 and NASA-80NSSC18K0594. We would like to thank Seth Jacobson for many helpful discussions on KBO formation and two anonymous reviewers for their comments.

Appendix A. Observations and parameters

Table A.2:

Density values used.

Name			Density (kg/m^3)	Diameter (km)	Source
Typhon	42355	2002 CR_{46}	600	157 ± 34	Stansberry et al. (2012)
Ceto	65489	2003 FX_{128}	1370	174 ± 17	Grundy et al. (2007)
Teharonhiawako	88611	2001 QT_{297}	600	178^{+33}_{-36}	Vilenius, E. et al. (2014)
		2001 QC_{298}	1140	235^{+21}_{-23}	Vilenius, E. et al. (2014)
Altjira	148780	2001 UQ_{18}	300	123^{+19}_{-69}	Vilenius, E. et al. (2014)
Sila	79360	1997 CS_{29}	730	249^{+30}_{-31}	Vilenius, E. et al. (2014)
Lempo	47171	1999 TC_{36}	500	304 ± 101	Stansberry et al. (2006)
	55637	2002 UX_{25}	820	652 ± 12	Brown (2013)
Varda	174567	2003 MW_{12}	1270	705^{+81}_{-75}	Vilenius, E. et al. (2014)
Salacia	120347	2004 SB_{60}	1260	866 ± 37	Brown and Butler (2017)
Orcus	90482	2004 DW	1520	958 ± 23	Fornasier, S. et al. (2013)

Name			Density (kg/m^3)	Diameter (km)	Source
Quaoar	50000	2002 LM_{60}	2180	1070 ± 38	Vilenius, E. et al. (2014)
Charon			1700	1212 ± 2	Nimmo et al. (2016)
Haumea	136108	2003 EL_{61}	1885	1595 ± 11	Ortiz et al. (2017)
Eris	136199	2003 UB_{313}	2520	2326 ± 12	Brown et al. (2011)
Pluto	134340		1850	2376 ± 3	Nimmo et al. (2016)
Triton			2060	2706 ± 1.8	Thomas (2000)

Table A.3:

Radioactive isotope values used. Long lived isotope values from Robuchon and Nimmo (2011). Short lived isotope values from Castillo-Rogez et al. (2007) and Castillo-Rogez et al. (2009). Concentration is the abundance of that element relative within the silicate. For ^{60}Fe we use the value from Tang and Dauphas (2012).

Isotope	Concentration (ppb)	Specific heat production (W/kg)	Half-life (yrs)
^{235}U	5.4	568.7×10^{-6}	7.04×10^{8}
^{238}U	19.9	94.65×10^{-6}	4.47×10^{9}
^{40}K	737.9	29.17×10^{-6}	1.28×10^{9}
^{232}Th	38.7	26.38×10^{-6}	1.4×10^{10}
^{26}Al	600	0.355	7.16×10^{5}
^{60}Fe	100	7.0×10^{-2}	1.5×10^{6}
^{53} Mn	25.7	2.7×10^{-2}	3.7×10^{6}

Appendix B. Thermal model details

This section details the methods used in our numerical model. Everything in this section is consistent with the description in Bierson et al. (2018). For differences between this model and Bierson et al. (2018) see Section 2.

To account for the radial variation in conductivity (k), layer thickness (Δz), and density (ρ) of each grid point (subscript i), we use the heat conduction equation from (Kieffer, 2013) modified to spherical geometry. The following equation is derived in Bierson et al. (2018).

$$\Delta T_i = \frac{-2\Delta t}{\rho_i C p_i \Delta z_i r_i^2}\left[r_{i+1/2}^2 \frac{T_{i+1}-T_i}{\frac{\Delta z_{i+1}}{k_{i+1}}+\frac{\Delta z_i}{k_i}} - r_{i-1/2}^2 \frac{T_i - T_{i-1}}{\frac{\Delta z_{i-1}}{k_{i-1}}+\frac{\Delta z_i}{k_i}}\right]. \quad \text{(B.1)}$$

Here Δt is the model timestep and r_i is the radial location of the cell i.

As pore space closes the local density and therefore the layer thickness will change. To calculate the change in layer thickness it is convenient to define a quantity, Ψ, that is the ratio of the initial and final layer density

$$\Psi = \frac{\rho_0}{\rho_f}. \tag{B.2}$$

As derived in Bierson et al. (2018), Ψ is related to the change in the radial position of the top of the layer (ΔR) in terms of the initial layer thickness (Δz_0) and the original location of the layer top ($R_{t,0}$) assuming a fixed bottom boundary.

$$\Delta R_t = \left\{ \left[\left(1 - \frac{\Delta z_0}{R_{t,0}} \right)^3 \left(1 - \Psi \right) + \Psi \right]^{1/3} - 1 \right\} R_{t,0} \tag{B.3}$$

After a layer expands or contracts the radial position of all the layers above needs to be adjusted accordingly. The spherical geometry causes the change in the radial position of the layer bottom (Δa) to be different from the change of the radial position of the layer top (Δb). For the layer immediately above the layer that has changed density, $\Delta R = \Delta a$. With this constraint, and conservation of volume, we can calculate the change in layer thickness ($\Delta(\Delta z)$) for each layer above the layer that changed density.

$$\Delta b = \left\{ \left[\left(1 + \frac{\Delta a - \Delta z_0}{R_{t,0}} \right) - \left(1 - \frac{\Delta z}{R_{t,0}} \right)^3 \right]^{1/3} - 1 \right\} R_{t,0} \tag{B.4}$$

$$\Delta(\Delta z) = \Delta b - \Delta a \tag{B.5}$$

Because the radial position of each layer, R, is assumed to be at the layer center (not the center of mass), the change in the layer center is given as

$$\Delta R = \frac{\Delta a + \Delta b}{2} \tag{B.6}$$

The model Δt is recalculated at the start of each timestep using the Courant criterion as

$$\Delta t = 0.3 \min\left(\Delta z_i^2 \rho_i C p_i / k_i \right). \tag{B.7}$$

Appendix C. Mass loss during formation

In Bierson et al. (2018) it was suggested that the gravitational potential energy of a forming KBOs could cause a density gradient with size. The idea is that if accretion is sufficiently rapid, the surface temperatures could exceed the melting point of water ice. At this point a temporary atmosphere would form in vapor pressure equilibrium with the liquid surface. Given the low gravity of KBOs this atmosphere would be rapidly lost via hydrodynamic escape. The very fast accretion times of the gravitational collapse model (~100 yrs) made this plausible (Nesvorný et al., 2010). Because the gravitational potential energy scales roughly as r^5 we suggested that much more water could be driven off larger KBOs, leading to their higher density. In this appendix we construct a model for this process and find it cannot significantly affect the bulk density of KBOs.

Following the work of Kuramoto and Matsui (1994), we can write the energy balance of a forming KBO following

$$\underbrace{\frac{GM\dot{M}}{r}}_{\text{Gravitational potential energy}} = \underbrace{4\pi r^2\sigma T^4}_{\text{Blackbody radiation}} + \underbrace{C_p\dot{M}\left(T-T_0\right)}_{\text{Warming incomming material}} + \underbrace{C_p f M\dot{T}}_{\text{Warming surface layer}} + \underbrace{\Phi\left(T\right)\left(L_v+\frac{GM}{R}\right)}_{\text{Mass loss}} \quad \text{(C.1)}$$

Here dots indicate time derivative, M is the object mass, r is the radius, σ is the Stefan-Boltzmann constant, T is the surface temperature, C_p is the specific heat at constant pressure, T_0 is the temperature of objects before accretion, f is the fraction of the body mass in equilibrium with the surface temperature, L_v is latent heat of vaporization, and $\Phi(T)$ is the hydrodynamic escape rate (kg/s) assuming an isothermal atmosphere (Catling and Kasting, 2017). This formulation assumes internal thermal diffusion is not important on the timescale of formation. It also ignores the energy input from solar radiation which would effectively set a lower limit on the temperature. We solve Equation C.1 by assuming a function for $\dot{M}$. We found through sensitivity testing that the resulting temperature distribution is very insensitive to the chosen form of $\dot{M}$. For the results presented here we use the following equation from (Kuramoto and Matsui, 1994).

$$\dot{M} = 7.15\left(\frac{M}{M_f}\right)^{2/3}\frac{M_f - M}{\tau} \quad \text{(C.2)}$$

Here M_f is the final satellite mass and τ is the accretion time.

The results of this modeling are shown in Figure C.3. In agreement with Kuramoto and Matsui (1994) we find that the most loss occurs around a formation timescale of ~10^4 years. This is because this timescale balances the requirement that the energy delivery rate be high enough while providing a relatively long period over which escape can occur. We find however that very little mass is lost as most of the energy goes into warming the material from the cold background temperature (40 K). Lowering the initial density further to try and match the observed density of small KBOs would further reduce the energy budget and allow for even less mass loss than is shown here. From this we conclude that this process of accretional heating followed by hydrodynamic escape could not have significantly contributed to the density contrast observed in KBOs.

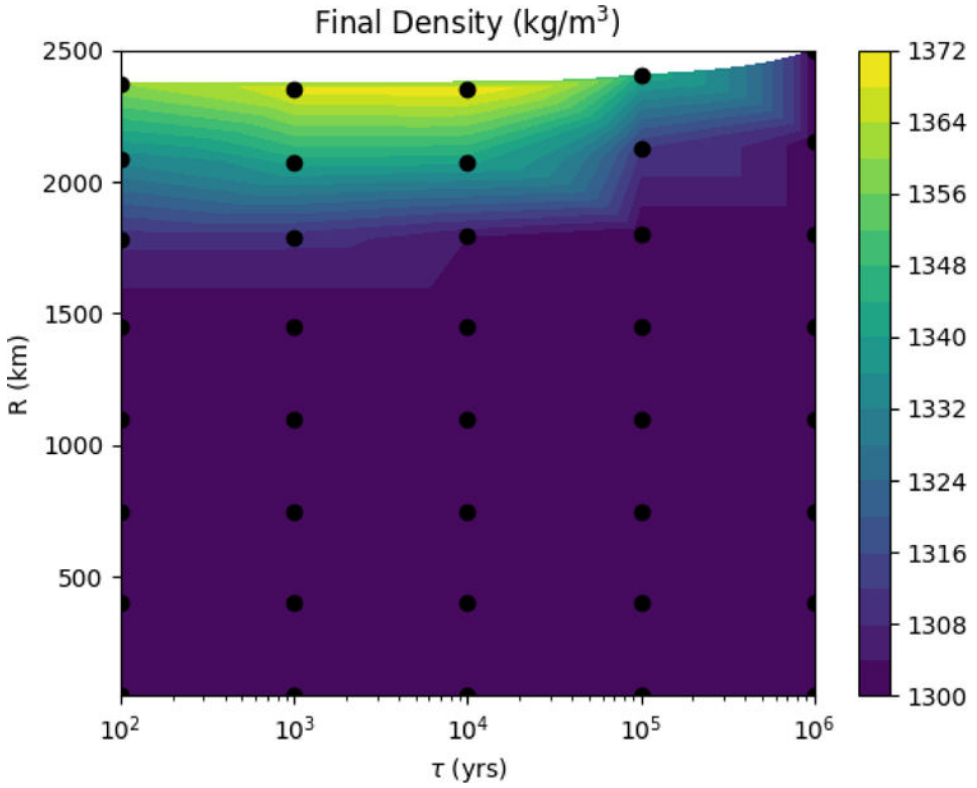

Figure C.3:
Final density obtained after integrating Equation C.1. Black dots are individual model runs. The initial material density used is 1300 kg/m^3 and the background temperature is 40K. Even in ideal conditions (large objects forming in ~10^4 yrs) very small changes in the final bulk density are found.

References

Agnor CB, Hamilton DP, 2006 Neptune's capture of its moon triton in a binary-ĂŞplanet gravitational encounter. Nature 441, 192–. URL: 10.1038/nature04792. [PubMed: 16688170]

Baer J, Chesley SR, Matson RD, 2011 Astrometric masses of 26 asteroids and observations on asteroid porosity. The Astronomical Journal 141, 143 URL: http://stacks.iop.org/1538-3881/141/i=5/a=143.

Barr AC, Schwamb ME, 2016 Interpreting the densities of the kuiper belt's dwarf planets. Monthly Notices of the Royal Astronomical Society 460, 1542–1548. URL: 10.1093/mnras/stw1052, doi:10.1093/mnras/stw1052.

Besserer J, Nimmo F, Roberts JH, Pappalardo RT, 2013 Convection-driven compaction as a possible origin of enceladus's long wavelength topography. Journal of Geophysical Research: Planets 118, 908–915. URL: 10.1002/jgre.20079, doi:10.1002/jgre.20079 note that there is an error in equation 2b.

Bierson C, Nimmo F, McKinnon W, 2018 Implications of the observed pluto-charon density contrast. Icarus 309, 207–219. URL: https://www.sciencedirect.com/science/article/pii/S0019103517303081, doi:10.1016/j.icarus.2018.03.007.

Brown ME, 2012 The compositions of kuiper belt objects. Annual Review of Earth and Planetary Sciences 40, 467–494. URL: 10.1146/annurev-earth-042711-105352, doi:10.1146/annurev-earth-042711-105352, arXiv:10.1146/annurev-earth-042711-1

Brown ME, 2013 The density of mid-sized kuiper belt object 2002 ux25 and the formation of the dwarf planets. The Astrophysical Journal Letters 778, L34 URL: http://stacks.iop.org/2041-8205/778/i=2/a=L34.

Brown ME, Burgasser AJ, Fraser WC, 2011 The surface composition of large kuiper belt object 2007 or10. The Astrophysical Journal Letters 738, L26 URL: http://stacks.iop.org/2041-8205/738/i=2/a=L26.

Brown ME, Butler BJ, 2017 The density of mid-sized kuiper belt objects from alma thermal observations. The Astronomical Journal 154, 19 URL: http://stacks.iop.org/1538-3881/154/i=1/a=19.

Canup RM, 2011 On a giant impact origin of charon, nix, and hydra. The Astronomical Journal 141, 35 URL: http://stacks.iop.org/1538-3881/141/i=2/a=35.

Carson JK, Lovatt SJ, Tanner DJ, Cleland AC, 2005 Thermal conductivity bounds for isotropic, porous materials. International Journal of Heat and Mass Transfer 48, 2150–2158. URL: http://www.sciencedirect.com/science/article/pii/S0017931005000670, doi:10.1016/j.ijheatmasstransfer.2004.12.032.

Castillo-Rogez J, Johnson TV, Lee MH, Turner NJ, Matson DL, Lunine J, 2009 26al decay: Heat production and a revised age for iapetus. Icarus 204, 658–662. URL: www.sciencedirect.com/science/article/pii/S0019103509003248, doi:10.1016/j.icarus.2009.07.025.

Castillo-Rogez J, Matson D, Sotin C, Johnson T, Lunine J, Thomas P, 2007 Iapetus' geophysics: Rotation rate, shape, and equatorial ridge. Icarus 190, 179–202. URL: http://www.sciencedirect.com/science/article/pii/S0019103507001108, doi:10.1016/j.icarus.2007.02.018.

Catling DC, Kasting JF, 2017 Escape of Atmospheres to Space. Cambridge University Press p. 129? 168. doi:10.1017/9781139020558.006.

Dalle Ore CM, Dalle Ore LV, Roush TL, Cruikshank DP, Emery JP, Pinilla-Alonso N, Marzo GA, 2013 A compositional interpretation of trans-neptunian objects taxonomies. Icarus 222, 307–322. URL: http://www.sciencedirect.com/science/article/pii/S0019103512004617, doi:10.1016/j.icarus.2012.11.015.

Desch SJ, Cook JC, Doggett T, Porter SB, 2009 Thermal evolution of kuiper belt objects, with implications for cryovolcanism. Icarus 202, 694–714. URL: http://www.sciencedirect.com/science/article/pii/S0019103509001146, doi:10.1016/j.icarus.2009.03.009.

Durham WB, McKinnon WB, Stern LA, 2005 Cold compaction of water ice. Geophysical Research Letters 32 URL: 10.1029/2005GL023484, doi:10.1029/2005GL023484.l18202.

Eluszkiewicz J, 1990 Compaction and internal structure of mimas. Icarus 84, 215–225. URL: http://www.sciencedirect.com/science/article/pii/0019103590901678, doi:10.1016/0019-1035(90)90167-8.

Fornasier S, Lellouch E, Müller T, Santos-Sanz P, Panuzzo P, Kiss C, Lim T, Mommert M, Bockelée-Morvan D, Vilenius E, Stansberry J, Tozzi GP, Mottola S, Delsanti A, Crovisier J, Duffard R, Henry F, Lacerda P, Barucci A, Gicquel A, 2013 Tnos are cool: A survey of the trans-neptunian region - viii. combined herschel pacs and spire observations of nine bright targets at 70–500 μm. A&A 555, A15 URL: 10.1051/0004-6361/201321329, doi:10.1051/0004-6361/201321329.

Fraser WC, Bannister MT, Pike RE, Marsset M, Schwamb ME, Kavelaars JJ, Lacerda P, NesvornÃ¡ D, Volk K, Delsanti A, Benecchi S, Lehner MJ, Noll K, Gladman B, Petit JM, Gwyn S, Chen YT, Wang SY, Alexandersen M, Burdullis T, Sheppard S, Trujillo C, 2017 All planetesimals born near the kuiper belt formed as binaries. Nature Astronomy 1, 0088–. URL: 10.1038/s41550-017-0088.

Goldreich P, Lithwick Y, Sari R, 2002 Formation of kuiper-belt binaries by dynamical friction and three-body encounters. Nature 420, 643–. URL: 10.1038/nature01227. [PubMed: 12478286]

Goldreich P, Murray N, Longaretti PY, Banfield D, 1989 Neptune's story. Science 245, 500–504. URL: http://science.sciencemag.org/content/245/4917/500, doi:10.1126/science.245.4917.500, arXiv:http://science.sciencemag.org/content/245/4917/500.full [PubMed: 17750259]

Grimm RE, McSween HY Jr, 1993 Heliocentric zoning of the asteroid belt by aluminum-26 heating. Science, 653–655 URL: http://www.jstor.org/stable/2882870?seq=1. [PubMed: 8235584]

Grundy W, Stansberry J, Noll K, Stephens D, Trilling D, Kern S, Spencer J, Cruikshank D, Levison H, 2007 The orbit, mass, size, albedo, and density of (65489) ceto/phorcys: A tidally-evolved binary

centaur. Icarus 191, 286–297. URL: http://www.sciencedirect.com/science/article/pii/S0019103507001546, doi:10.1016/j.icarus.2007.04.004.

Haisch KE Jr., Lada EA, Lada CJ, 2001 Disk frequencies and life-times in young clusters. The Astrophysical Journal Letters 553, L153 URL: http://stacks.iop.org/1538-4357/553/i=2/a=L153.

Johnson BC, Walsh KJ, Minton DA, Krot AN, Levison HF, 2016 Timing of the formation and migration of giant planets as constrained by cb chondrites. Science Advances 2 URL: http://advances.sciencemag.org/content/2/12/e1601658, doi:10.1126/sciadv.1601658, arXiv:http://advances.sciencemag.org/content/2/12/e1601658.full.pd

Jorda L, Gaskell R, Capanna C, Hviid S, Lamy P, eurech J, Faury G, Groussin O, Gutiérrez P, Jackman C, Keihm S, Keller H, Knollenberg J, Kührt E, Marchi S, Mottola S, Palmer E, Schloerb F, Sierks H, Vincent JB, A'Hearn M, Barbieri C, Rodrigo R, Koschny D, Rickman H, Barucci M, Bertaux J, Bertini I, Cremonese G, Deppo VD, Davidsson B, Debei S, Cecco MD, Fornasier S, Fulle M, Güttler C, Ip WH, Kramm J, Küppers M, Lara L, Lazzarin M, Moreno JL, Marzari F, Naletto G, Oklay N, Thomas N, Tubiana C, Wenzel KP, 2016 The global shape, density and rotation of comet 67p/churyumov-gerasimenko from preperihelion rosetta/osiris observations. Icarus 277, 257–278. URL: http://www.sciencedirect.com/science/article/pii/S0019103516301385, doi:10.1016/j.icarus.2016.05.002.

Kenyon SJ, 2002 Planet formation in the outer solar system. Publications of the Astronomical Society of the Pacific 114, 265 URL: http://stacks.iop.org/1538-3873/114/i=793/a=265.

Kenyon SJ, Bromley BC, O'Brien DP, Davis DR, 2008 Formation and collisional evolution of kuiper belt objects. The Solar System Beyond Neptune 293.

Kieffer H, 2013 Thermal model for analysis of mars infrared mapping. Journal of Geophysical Research: Planets 118, 451–470. URL: 10.1029/2012JE004164, doi:10.1029/2012JE004164.

Kiss C, Marton G, Farkas-Takács A, Stansberry J, Müller T, Vinkó J, Balog Z, Ortiz JL, Pál A, 2017 Discovery of a satellite of the large transneptunian object (225088) 2007 or 10. The Astrophysical Journal Letters 838, L1 URL: http://stacks.iop.org/2041-8205/838/i=1/a=L1.

Kruijer TS, Burkhardt C, Budde G, Kleine T, 2017 Age of jupiter inferred from the distinct genetics and formation times of meteorites. Proceedings of the National Academy of Sciences 114, 6712–6716. URL: http://www.pnas.org/content/114/26/6712, doi:10.1073/pnas.1704461114, arXiv:http://www.pnas.org/content/114/26/6712.full.pdf.

Kuramoto K, Matsui T, 1994 Formation of a hot proto-atmosphere on the accreting giant icy satellite: Implications for the origin and evolution of titan, ganymede, and callisto. Journal of Geophysical Research: Planets 99, 21183–21200. URL: 10.1029/94JE01864, doi:10.1029/94JE01864.

Leinhardt ZM, Marcus RA, Stewart ST, 2010 The formation of the collisional family around the dwarf planet haumea. The Astrophysical Journal 714, 1789 URL: http://stacks.iop.org/0004-637X/714/i=2/a=1789.

Leliwa-Kopystyński J, Kossacki K, 2000 Evolution of porosity in small icy bodies. Planetary and Space Science 48, 727–745. URL: http://www.sciencedirect.com/science/article/pii/S0032063300000386, doi:10.1016/S0032-0633(00)00038-6.

Lissauer JJ, Stewart GR, 1993 Growth of planets from planetesimals, in: Levy EH, Lunine JI (Eds.), Protostars and Planets III, pp. 1061–1088.

Malamud U, Prialnik D, 2015 Modeling kuiper belt objects charon, orcus and salacia by means of a new equation of state for porous icy bodies. Icarus 246, 21–36.

Matsuyama I, Johnstone D, Hartmann L, 2003 Viscous diffusion and photoevaporation of stellar disks. The Astrophysical Journal 582, 893 URL: http://stacks.iop.org/0004-637X/582/i=2/a=893.

McKinnon WB, Mueller S, 1988 Pluto's structure and composition suggest origin in the solar, not a planetary, nebula. Nature 335, 240–. URL: 10.1038/335240a0.

McKinnon WB, Stern S, Weaver H, Nimmo F, Bierson C, Cook J, Grundy W, Cruikshank D, Parker A, Moore J, Spencer J, Young L, Olkin C, Smith KE, 2017 Origin of the pluto-charon system: Constraints from the new horizons yby. Icarus, –URL: http://www.sciencedirect.com/science/article/pii/S0019103516307473, doi:10.1016/j.icarus.2016.11.019.

Merk R, Prialnik D, 2006 Combined modeling of thermal evolution and accretion of trans-neptunian objects-occurrence of high temperatures and liquid water. Icarus 183, 283–295. URL: http://

www.sciencedirect.com/science/article/pii/S0019103506000741, doi:10.1016/j.icarus.2006.02.011.

Milbury C, Johnson BC, Melosh HJ, Collins GS, Blair DM, Soderblom JM, Nimmo F, Bierson CJ, Phillips RJ, Zuber MT, 2015 Preimpact porosity controls the gravity signature of lunar craters. Geophysical Research Letters 42 URL: 10.1002/2015GL066198, doi:10.1002/2015GL066198.

Nesvorný D, Youdin AN, Richardson DC, 2010 Formation of kuiper belt binaries by gravitational collapse. The Astronomical Journal 140, 785 URL: http://stacks.iop.org/1538-3881/140/i=3/a=785.

Nimmo F, Umurhan O, Lisse CM, Bierson CJ, Lauer TR, Buie MW, Throop HB, Kammer JA, Roberts JH, McKinnon WB, Zangari AM, Moore JM, Stern SA, Young LA, Weaver HA, Olkin CB, Ennico K, 2016 Mean radius and shape of pluto and charon from new horizons images. Icarus, – URL: http://www.sciencedirect.com/science/article/pii/S0019103516303529, doi:10.1016/j.icarus.2016.06.027.

Ortiz JL, Santos-Sanz P, Sicardy B, Benedetti-Rossi G, Bérard D, Morales N, Duffard R, Braga-Ribas F, Hopp U, Ries C, Nascimbeni V, Marzari F, Granata V, Pál A, Kiss C, Pribulla T, Komžík R, Hornoch K, Pravec P, Bacci P, Maestripieri M, Nerli L, Mazzei L, Bachini M, Martinelli F, Succi G, Ciabattari F, Mikuz H, Carbognani A, Gaehrken B, Mottola S, Hellmich S, Rommel FL, Fernádez-Valenzuela E, Bagatin AC, Cikota S, Cikota A, Lecacheux J, Vieira-Martins R, Camargo JIB, Assafin M, Colas F, Behrend R, Desmars J, Meza E, Alvarez-Candal A, Beisker W, Gomes-Junior AR, Morgado BE, Roques F, Vachier F, Berthier J, Mueller TG, Madiedo JM, Unsalan O, Sonbas E, Karaman N, Erece O, Koseoglu DT, Ozisik T, Kalkan S, Guney Y, Niaei MS, Satir O, Yesilyaprak C, Puskullu C, Kabas A, Demircan O, Alikakos J, Charmandaris V, Leto G, Ohlert J, Christille JM, Szakáts R, Farkas AT, Varga-Verebélyi E, Marton G, Marciniak A, Bartczak P, Santana-Ros T, Butkiewicz-Bąk M, DudzińĎski G, Alí-Lagoa V, Gazeas K, Tzouganatos L, Paschalis N, Tsamis V, Sánchez-Lavega A, Pérez-Hoyos S, Hueso R, Guirado JC, Peris V, Iglesias-Marzoa R, 2017 The size, shape, density and ring of the dwarf planet haumea from a stellar occultation. Nature 550, 219–. URL: 10.1038/nature24051. [PubMed: 29022593]

Parker AH, Buie MW, Grundy WM, Noll KS, 2016 Discovery of a makemakean moon. The Astrophysical Journal Letters 825, L9 URL: http://stacks.iop.org/2041-8205/825/i=1/a=L9.

Petit JM, Mousis O, 2004 Kbo binaries: how numerous were they? Icarus 168, 409–419. URL: http://www.sciencedirect.com/science/article/pii/S0019103503004330, doi:10.1016/j.icarus.2003.12.013.

Rivoldini A, Hoolst TV, Verhoeven O, 2009 The interior structure of mercury and its core sulfur content. Icarus 201, 12–30. URL: http://www.sciencedirect.com/science/article/pii/S001910350800448X, doi:10.1016/j.icarus.2008.12.020.

Robuchon G, Nimmo F, 2011 Thermal evolution of pluto and implications for surface tectonics and a subsurface ocean. Icarus 216, 426–439. URL: http://www.sciencedirect.com/science/article/pii/S0019103511003320, doi:10.1016/j.icarus.2011.08.015.

Satorre M, Domingo M, Millán C, Luna R, Vilaplana R, Santonja C, 2008 Density of ch4, n2 and co2 ices at different temperatures of deposition. Planetary and Space Science 56, 1748–1752. URL: http://www.sciencedirect.com/science/article/pii/S0032063308002304, doi:10.1016/j.pss.2008.07.015 advances in Planetary Sciences: AOGS 20074th Annual Meeting of the.

Satorre M, Leliwa-Kopystynski J, Santonja C, Luna R, 2013 Refractive index and density of ammonia ice at different temperatures of deposition. Icarus 225, 703–708. URL: http://www.sciencedirect.com/science/article/pii/S0019103513001887, doi:10.1016/j.icarus.2013.04.023.

Saxena P, Renaud JP, Henning WG, Jutzi M, Hurford T, 2018 Relevance of tidal heating on large tnos. Icarus 302, 245–260. URL: http://www.sciencedirect.com/science/article/pii/S0019103517303858, doi:10.1016/j.icarus.2017.11.023.

Schlichting HE, Sari R, 2011 Runaway growth during planet formation: Explaining the size distribution of large kuiper belt objects. The Astrophysical Journal 728, 68 URL: http://stacks.iop.org/0004-637X/728/i=1/a=68.

Shoshany Y, Prialnik D, Podolak M, 2002 Monte carlo modeling of the thermal conductivity of porous cometary ice. Icarus 157, 219–227. URL: http://www.sciencedirect.com/science/article/pii/S0019103502968156, doi:10.1006/icar.2002.6815.

Stansberry J, Grundy W, Mueller M, Benecchi S, Rieke G, Noll K, Buie M, Levison H, Porter S, Roe H, 2012 Physical properties of trans-neptunian binaries (120347) salacia-actaea and (42355) typhon-echidna. Icarus 219, 676–688. URL: http://www.sciencedirect.com/science/article/pii/S0019103512001224, doi:10.1016/j.icarus.2012.03.029.

Stansberry JA, Grundy WM, Margot JL, Cruikshank DP, Emery JP, Rieke GH, Trilling DE, 2006 The albedo, size, and density of binary kuiper belt object (47171) 1999 tc36. The Astrophysical Journal 643, 556 URL: http://stacks.iop.org/0004-637X/643/i=1/a=556.

Tang H, Dauphas N, 2012 Abundance, distribution, and origin of 60fe in the solar protoplanetary disk. Earth and Planetary Science Letters 359–360, 248–263. URL: http://www.sciencedirect.com/science/article/pii/S0012821X12005705, doi:10.1016/j.epsl.2012.10.011.

Tegler SC, Romanishin W, Consolmagno GJ, S.J, 2016 Two color populations of kuiper belt and centaur objects and the smaller orbital inclinations of red centaur objects. The Astronomical Journal 152, 210 URL: http://stacks.iop.org/1538-3881/152/i=6/a=210.

Thomas P, 2000 The shape of triton from limb profiles. Icarus 148, 587–588. URL: http://www.sciencedirect.com/science/article/pii/S0019103500965114, doi:10.1006/icar.2000.6511.

Umurhan O, Howard A, Moore J, Earle A, White O, Schenk P, Binzel R, Stern S, Beyer R, Nimmo F, McKinnon W, Ennico K, Olkin C, Weaver H, Young L, 2017 Modeling glacial flow on and onto pluto's sputnik planitia. Icarus 287, 301–319. URL: http://www.sciencedirect.com/science/article/pii/S0019103517300489, doi:10.1016/j.icarus.2017.01.017 special Issue: The Pluto System.

Vilenius E, Kiss C, Müller T, Mommert M, Santos-Sanz P, Pál A, Stansberry J, Mueller M, Peixinho N, Lellouch E, Fornasier S, Delsanti A, Thirouin A, Ortiz JL, Duffard R, Perna D, Henry F, 2014 "tnos are cool": A survey of the trans-neptunian region - x. analysis of classical kuiper belt objects from herschel and spitzer observations. A&A 564, A35 URL: 10.1051/0004-6361/201322416, doi:10.1051/0004-6361/201322416.

Wang H, Weiss BP, Bai XN, Downey BG, Wang J, Wang J, Suavet C, Fu RR, Zucolotto ME, 2017 Lifetime of the solar nebula constrained by meteorite paleomagnetism. Science 355, 623–627. URL: http://science.sciencemag.org/content/355/6325/623, doi:10.1126/science.aaf5043, arXiv:http://science.sciencemag.org/content/355/6325/623.full.pdf. [PubMed: 28183977]

Weber RC, Lin PY, Garnero EJ, Williams Q, Lognonné P, 2011 Seismic detection of the lunar core. Science 331, 309–312. URL: http://science.sciencemag.org/content/331/6015/309, doi:10.1126/science.1199375, arXiv:http://science.sciencemag.org/content/331/6015/309.full.pdf. [PubMed: 21212323]

Williams JP, Cieza LA, 2011 Protoplanetary disks and their evolution. Annual Review of Astronomy and Astrophysics 49, 67–117. URL: 10.1146/annurev-astro-081710-102548, doi:10.1146/annurev-astro-081710-102548, arXiv:10.1146/annurev-astro-081710-102

Yasui M, Arakawa M, 2009 Compaction experiments on icesilica particle mixtures: Implication for residual porosity of small icy bodies. Journal of Geophysical Research: Planets 114 URL: 10.1029/2009JE003374, doi:10.1029/2009JE003374.e09004.

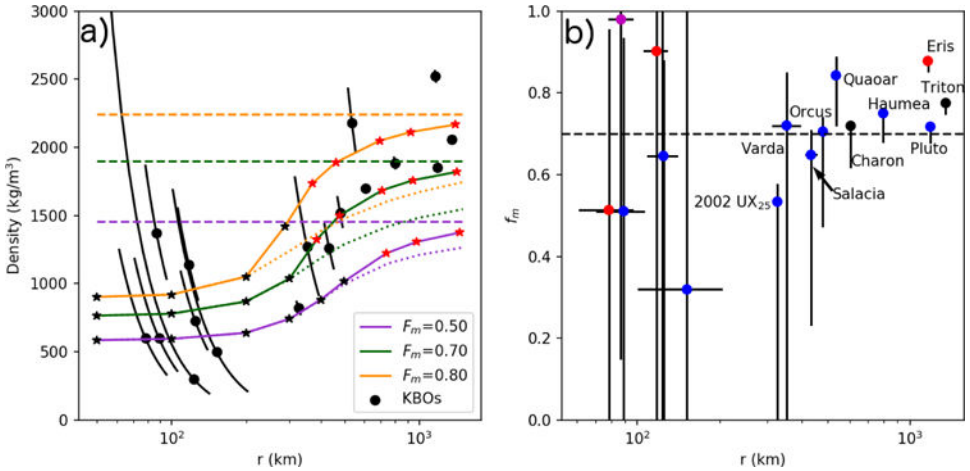

Figure 1:

a) Density of observed KBOs with 1σ errors in black. Error bars only account for uncertainty in radius. See Table A.2 for citations. Each color refers to a fixed rock mass fraction indicated in the legend. Flat dashed lines show the density of a non-porous object. Dotted line shows the expected density only accounting for brittle failure. Solid lines show model results that include the effects of thermally controlled viscous relaxation. Individual model runs are show with stars. Red stars indicate models where internal temperatures met or exceeded 250 K at some point. All thermal models were started at 10 Myr to avoid the effects of ^{26}Al decay (See Figure 2). b) Estimated rock mass fraction of each KBO by interpolating model runs. Horizontal line is $f_m = 0.7$. Colors indicate object class where blue are classical and resonant KBOs, red is scattered disk object, magenta is centaur, and black are satellites. The upper f_m limit is the interpolated model value using the 1σ density upper bound. The lower f_m limit is the f_m calculated assuming no porosity and the 1σ density lower bound.

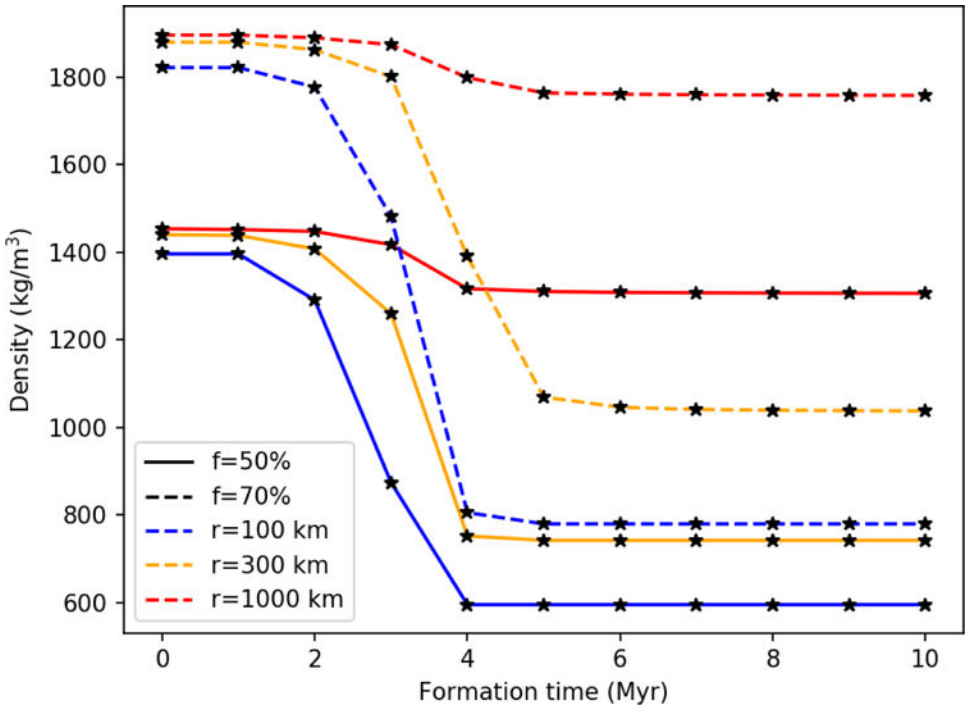

Figure 2:

Modeled final density of three KBOs of different sizes formed a different times after CAI. Models are shown with f_m=0.70 or 0.50 and with an initial temperature of 40 K. If any small (~100 km-scale) KBOs formed earlier than 4 Myr after CAI the heat from short lived radioisotopes would remove a significant fraction of their internal porosity.

Table 1:

Parameters used. Values for b_1, b_2 based on Yasui and Arakawa (2009). ϕ_c value based on Durham et al. (2005). Other parameter values are from Bierson et al. (2018).

	Symbol	Nominal Value	Units
Ice Reference Viscosity	η_0	10^{14}	Pa s
Viscosity Reference Temperature	T_0	270	K
Activation Energy	Q	60	kJ/mol
Ice Thermal Conductivity	k_{ice}	0.4685 + 488.12/T	W/(m K)
Silicate Thermal Conductivity	k_s	3.0	W/(m K)
Surface Temperature	T_s	40.0	K
Initial Temperature	T_0	100.0	K
Specific Heat	Cp	1000	J/(kg K)
Ice Density	ρ_{ice}	920	kg/m^3
Silicate Density	ρ_s	3500	kg/m^3
Initial Porosity	ϕ_0	0.60	
Strength supported porosity	ϕ_c	0.20	
Empirical compaction parameter (ice)	b_1	−0.1	MPa^{-1}
Empirical compaction parameter (silicate)	b_2	−0.11	